ACS APPLIED MATERIALS & INTERFACES

Research Article

www.acsami.org

Confining Iron Carbide Nanocrystals inside CN_x@CNT toward an Efficient Electrocatalyst for Oxygen Reduction Reaction

Yun Zhang,[†,‡] Wen-Jie Jiang,[‡] Lin Guo,[†,‡] Xing Zhang,[‡] Jin-Song Hu,*[,‡] Zidong Wei,*[,†] and Li-Jun Wan[‡]

[†]State Key Laboratory of Power Transmission Equipment & System Security and New Technology, College of Chemistry and Chemical Engineering, Chongqing University, Chongqing 400044, China

[‡]Beijing National Laboratory for Molecular Sciences, Key Laboratory of Molecular Nanostructure and Nanotechnology, Institute of Chemistry, Chinese Academy of Science, 2 North First Street, Zhongguancun, Beijing 100190, China

Supporting Information

ABSTRACT: The development of low-cost electrocatalysts with comparable activity for oxygen reduction reaction (ORR) to substitute platinum-based catalysts is imperative but still challenging for the commercialization of fuel cells. Herein, we reported a strategy to effectively confine iron carbide nanocrystals in N-doped carbon coated on carbon nanotubes (CN_x@CNT), which prevented the agglomeration of iron carbide during pyrolysis and thus provided the sufficient highly active catalytic sites. Together with the benefit from three-dimensional conductive network of CNT-based core−shell structure for fast electron transfer and rapid mass transfer, the developed nanocatalyst exhibited the significantly enhanced electrocatalytic activity for ORR, as well as high durability and methanol tolerance. Moreover, it was interestingly found that the types of the confined iron compounds appreciably affected the performance of the catalysts, and Fe_3C might be most effective on improving ORR activity in this case.

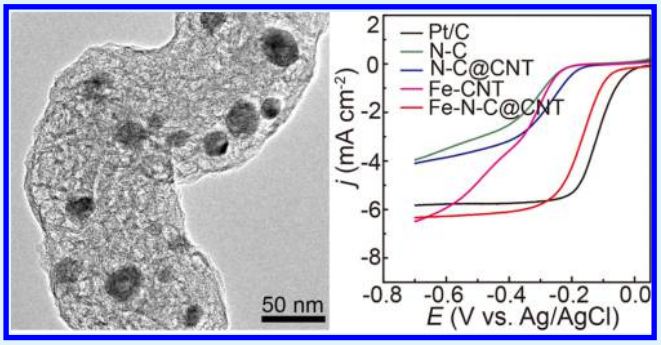

KEYWORDS: *oxygen reduction reaction, non-noble-metal catalysts, carbon nanotubes, iron carbides, nitrogen-doped carbon*

INTRODUCTION

Fuel cells, as efficient clean energy conversion devices, are promising for tackling the future global energy crisis and environmental issues.[1,2] However, the sluggish kinetics in cathode oxygen reduction reaction (ORR) still limits fuel cell performance, while the scarce and expensive Pt-based anode and cathode catalysts retard commercialization.[3−13] Therefore, it is necessary and urgent to develop low-cost electrocatalysts with sufficient activity for ORR as substitutes for Pt-based catalysts. Many efforts have been made to explore such catalysts, such as nonprecious transition metal (Fe, Co, etc.) based catalysts as well as some nonmetal element (B, N, S, etc.) doped carbon materials.[14−29] Among these materials, iron/nitrogen containing (Fe/N) carbon-based materials have been considered as one of the most promising non-noble-metal ORR catalysts due to the low cost, high activity, and excellent durability, especially for applications in alkaline fuel cells.[30−34]

Fe/N carbon-based ORR catalysts were generally prepared by directly pyrolyzing the composites of carbon/nitrogen-containing precursors such as phthalocyanin, cyanamide, polyaniline, melamine, and polydopamine with iron salt or complexes of iron and N_4-chelating ligands.[26,35−40] To improve the conductivity of the catalysts, graphitic carbon materials (graphene, carbon nanotubes, etc.) were frequently introduced to construct electrocatalyst composites. During most of these synthetic processes, the morphologies, composition, and structure of the catalysts were not controllable, and their influences on the catalytic performance were seldom investigated. It was reported that the rational design of catalyst architectures and careful regulation of interactions between active moieties and matrixes during in the synthetic process were important to maximize ORR catalytic performance.[40,41] In this study, we developed an effective strategy to prepare a new type of Fe/N containing core−shell carbon/carbon nanotube catalyst (Fe−N−C@CNT), in which well-defined iron carbide (Fe_xC) nanocrystals were encapsulated inside the N-doped carbon (CN_x) shell. The CN_x shell not only effectively prevented the aggregation and agglomeration of iron carbide nanocrystals, but also produced sufficient highly active sites for ORR by means of the interaction with iron carbide nanocrystals. The influence of synthetic conditions of the catalysts on the catalytic activity was further investigated, and it was found that the types of iron compounds appreciably affected the catalytic performance of the catalysts. Ascribed to the well-defined core−shell structure and the composition control of iron compounds, the designed Fe−N−C@CNT catalyst demonstrated the significantly enhanced electrocatalytic activity for ORR, as well as high durability and methanol tolerance.

Received: March 20, 2015
Accepted: May 18, 2015
Published: May 18, 2015

DOI: 10.1021/acsami.5b02467
ACS Appl. Mater. Interfaces 2015, 7, 11508−11515

RESULTS AND DISCUSSION

As shown in Figure 1a, a three-step strategy was applied to achieve well-defined Fe−N−C@CNT. In brief, Fe_3O_4 nanoparticles were first controllably loaded on CNT surface to get Fe_3O_4/CNT composite. Polydopamine (PDA) layer was then coated on Fe_3O_4/CNT to obtain the composite of PDA@Fe_3O_4/CNT, which was then converted into the Fe−N−C@CNT after pyrolysis at 800 °C. During pyrolysis, the PDA layer was decomposed into a CN_x layer, and Fe_3O_4 nanoparticles were reduced in situ to Fe_xC nanoparticles, which were well-confined in the CN_x layer. The typical scanning electron microscopy (SEM) image of Fe_3O_4/CNT in Figure 1b displayed that the entire surfaces of all CNT were covered by a layer of nanoparticles. Transmission electron microscopy (TEM) image (Figure 1c) further exhibited that the nanoparticles in a size of several nanometers were well dispersed on the CNT surfaces with no obvious aggregation. A representative high-resolution TEM (HRTEM) image (Figure 1c, inset) showed clear lattice fringes with a distance of 0.24 nm which is in good agreement with the *d*-spacing of (222) plane of cubic Fe_3O_4, indicating that these nanoparticles were Fe_3O_4 nanocrystals. X-ray diffraction (XRD) pattern of Fe_3O_4/CNT composite in Figure 1d clearly showed the typical peaks at 30.10, 35.45, 56.98, and 62.57° from cubic Fe_3O_4 (JCPDS no. 39-1346) and the peak at 26.60° from CNT, which corroborated that the composite was composed of cubic Fe_3O_4 and CNT.

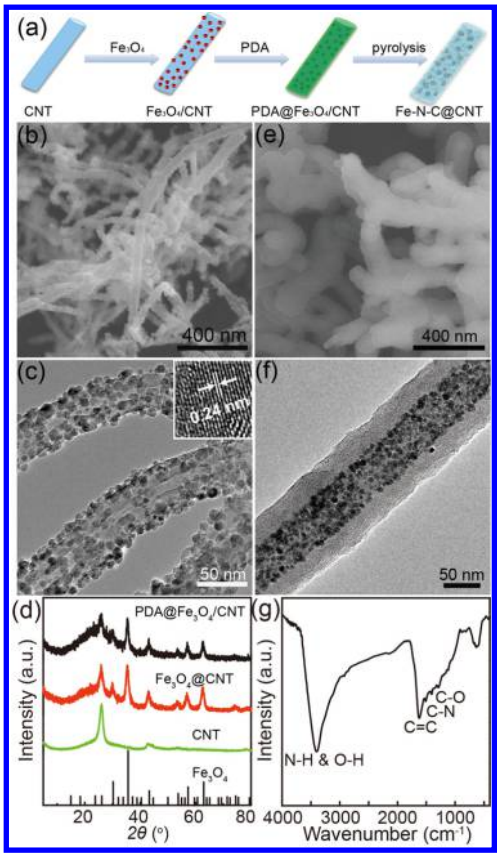

Figure 1. (a) Schematic illustration of the preparation of Fe−N−C@CNT. (b) Typical SEM and (c) TEM images of Fe_3O_4/CNT. (d) XRD patterns of CNT, Fe_3O_4/CNT, and PDA@ Fe_3O_4/CNT. (e) Typical SEM and (f) TEM images of PDA@Fe_3O_4/CNT (g) FTIR spectrum of PDA@ Fe_3O_4/CNT.

After the PDA coating, it can be seen from SEM image in Figure 1e that Fe_3O_4/CNT was uniformly coated with a layer with a smooth surface, and the diameter of nanotubes became larger. The TEM image in Figure 1f clearly displayed the core−shell structure of PDA@Fe_3O_4/CNT with a Fe_3O_4/CNT core and a PDA shell in ∼30 nm thick. No spherical structures from self-polymerization of dopamine were found during SEM and TEM observation, indicating that the hydrophilic surface of Fe_3O_4 favored the core−shell coating of PDA on Fe_3O_4/CNT cores. It should be noted that the thickness of the PDA layer could be easily controlled by the polymerization time (Figure S1a, SI). The thickness of the PDA shell was optimized by measuring their electrocatalytic activity, as discussed in the Experimental Section, and 30 nm thick PDA shells were used in the following experiments. The XRD pattern (Figure 1d, black curve) indicated that the PDA coating had a negligible influence on the crystalline structure of Fe_3O_4/CNT. Fourier transform infrared (FTIR) spectrum of PDA@Fe_3O_4/CNT (Figure 1g) showed the characteristic FTIR signals corresponding to the vibrations from functional groups of N−H, O−H, C−O, and C−N of PDA, corroborating that the shell shown in Figure 1f is PDA.

Figure 2a presented the typical SEM images of the final product after the pyrolysis of PDA@Fe_3O_4/CNT at 800 °C. A higher-magnification SEM image is shown in Figure S2 (SI). It can be seen that the morphology of one-dimensional nanotubes was well maintained after the pyrolysis. The nanoparticles in a brighter contrast were observed in the catalyst and seems to be covered by a layer of materials. No clear outer surface of these nanoparticles can be identified in the high-magnification SEM image, and no nanoparticles were found at the edges of the nanotubes in either SEM or TEM observations. In consideration of the fact the iron precursors were covered with the PDA layer (Figure 1f), it can be reasonably presumed that these nanoparticles were covered by the carbon layers derived from the pyrolysis of PDA but should still be on the outer surfaces of the inner nanotubes. Compared to Figure 1f, the TEM image of the pyrolyzed product (Figure 2b) clearly displayed that the smooth shell layer in PDA@Fe_3O_4/CNT was converted into a porous carbon layer with wrinkled folds from the decomposition and graphitization of PDA. The Fe_3O_4 nanocrystal layer was changed into larger nanoparticles in a size of 15−20 nm which decorated inside the carbon layer without obvious aggregation. The larger size could be due to the migration and ripening of the nanocrystals during the reduction. In contrast, the Fe_3O_4 nanocrystals in Fe_3O_4/CNT without the protection of PDA shell layer turned into larger aggregates and detached from CNT after the same heat treatment, as shown in the TEM image (Figure 2c). The thicker the PDA shell was, the more effective this space-confinement effect was. As shown in Figure S1b (SI), when the thickness of PDA shell increased to ∼90 nm, the size of the formed nanoparticles after the pyrolysis decreased, indicating less aggregation. Therefore, it could be concluded that the PDA shell effectively prevented the aggregation and growth of the reduced nanoparticles due to the space confinement effect. Moreover, the continuous lattice fringes throughout the whole nanoparticle shown in HRTEM image (Figure 2b, inset) implied that these nanoparticles were well crystallized. The distance of 0.21 nm between lattice fringes was consistent with the *d*-spacing of (211) planes of Fe_3C.

The nitrogen adsorption/desorption isothermal technique was further employed to characterize the porous nature of Fe−

DOI: 10.1021/acsami.5b02467
ACS Appl. Mater. Interfaces 2015, 7, 11508−11515

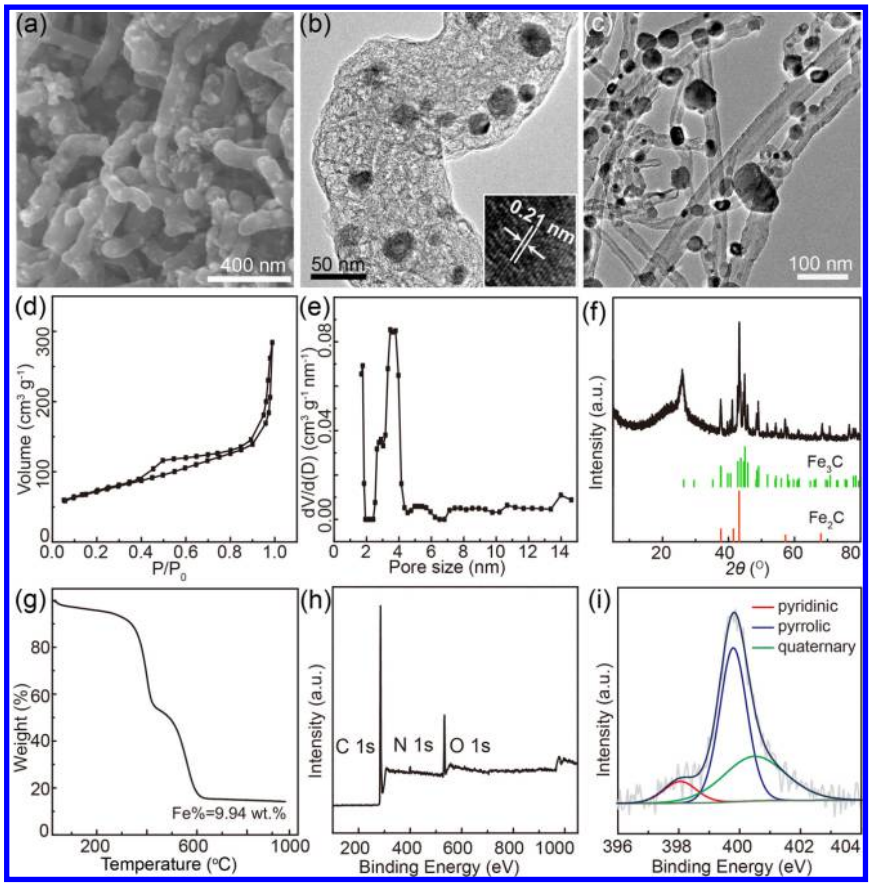

Figure 2. (a) Typical SEM and (b) TEM images of Fe−N−C@CNT. (c) Typical TEM image of Fe-CNT. (d) N_2 adsorption−desorption isotherm and (e) pore size distribution of Fe−N−C@CNT. (f) XRD pattern of Fe−N−C@CNT, Fe_3C, and Fe_2C. (g) TGA profile, (h) wide-scan survey XPS spectrum, and (i) high-resolution N 1s XPS signal of Fe−N−C@CNT.

N−C@CNT. The Brunauer−Emmett−Teller (BET) analysis (Figure 2d) showed that the Fe−N−C@CNT had a high surface area of 245.1 m^2/g, which is much larger than that of pristine CNT (79.5 m^2/g).[2] The corresponding pore size distribution curves (Figure 2e), calculated by the density functional theory (DFT), revealed the existence of a great quantity of nanopores less than 4 nm in the Fe−N−C@CNT. These nanopores could offer a large number of potential active sites for catalyzing ORR and supply abundant channels for the mass transfer of reactants and products.

XRD was further used to analyze the crystalline structure of these nanoparticles. The XRD pattern of Fe−N−C@CNT in Figure 2f showed a multitude of diffraction peaks. By looking into the XRD database, we found that the peaks at 37.74, 44.99, 45.86, and 49.15° could be well indexed to the characteristic diffraction of orthorhombic Fe_3C (JCPDS no. 35-0772) and the peaks at 37.68, 41.48, 43.23, and 68.03° could be ascribed to the hexagonal Fe_2C (JCPDS no. 36-1249). The peak at 26.60° was from the diffraction of (002) planes of graphitized carbon. All other weak peaks matched with the orthorhombic Fe_3C (JCPDS no. 35-0772) as well. These results evidenced that the nanocrystals in darker contrast in TEM image of Fe−N−C@CNT (Figure 2b) should be composed of Fe_3C and Fe_2C. The content of iron in the composite was further determined by thermogravimetric analysis (TGA). Figure 2g presented the TGA curve of Fe−N−C@CNT recorded under atmosphere; 14.21% of weight remained at above 600 °C, which could be ascribed to the formation of Fe_2O_3 during heating and corresponded to 9.94 wt % of iron.

Moreover, X-ray photoelectron spectroscopy (XPS) was employed to investigate the chemical bonding state of nitrogen in Fe−N−C@CNT. As shown in Figure 2h, the N 1s signal in XPS survey spectrum of Fe−N−C@CNT indicated the successful introduction of N into the composite. The nitrogen content was calculated to be 1.68 at. %. To clearly investigate the bonding state of nitrogen, we deconvoluted the high-resolution N 1s signal into three typical components (~398.05 eV for pyridinic N, ~399.79 eV for pyrrolic N, and ~400.49 eV for quaternary N), as shown in Figure 2i. The content for each type of N was 9.28, 54.78, and 35.94 at. %, respectively. On the other hand, the iron signal in the survey scan XPS spectrum was very weak, and the iron content calculated on a basis of XPS signal was just ~0.17 at. %, far from the TGA result. Compared with the TGA result (9.94 wt %, Figure 2g), such a low content of iron on the surface implied that most iron carbide nanoparticles were buried in the carbon shell.

It was reported that transition metal-based nanoparticles was able to enhance the electrocatalytic performance of carbon materials.[33,38,41−45] For example, Bao's groups found that the Fe nanoparticles encapsulated inside CNT could improve the catalytic activity for ORR.[33] Based on DFT calculations, they attributed the improvement to the decrease of local work function on the carbon surfaces due to the electron transfer from the encapsulated Fe nanoparticles to the surface of CNT. If nitrogen was introduced into the carbon lattice, the local work function was further reduced, resulting in the significant enhancement of catalytic performance. Xing's group reported that Fe_3C nanoparticles in the carbon layers did not participate

DOI: 10.1021/acsami.5b02467
ACS Appl. Mater. Interfaces 2015, 7, 11508−11515

in ORR directly, but still played a key role in the catalysis by activating the surrounding graphitic layers.[41] Recently, Deng's group ascribed the superior HER performance of CoNi@NC material to the modification of the electron density and the electronic potential distribution at the carbon surfaces by a penetrating electron from the CoNi cores.[43] All of the above literatures indicated that the improvement of electrocatalytic performance from transition metal-based nanoparticles could stem from the unique electronic interaction between the confined nanoparticles and the carbon shells; and the encased nanoparticles did not take part in the catalytic reaction while the modulated carbon layers supplied the efficient active sites for catalyzing ORR or HER.

In the present Fe−N−C@CNT, iron carbide nanocrystals were well confined inside the porous N-doped carbon/CNT, as discussed above, in which iron carbide nanocrystals encapsulated with the porous N-doped carbon could act as highly active sites, and CNT core could be used as efficient conductive network for fast electron transfer. This structure was expected to exhibit the superior performance. The electrocatalytic performance for ORR of Fe−N−C@CNT was first evaluated by linear sweep voltammetry (LSV) technique. Several other catalysts prepared in parallel and commercial Johnson Matthey Pt/C catalyst (20 wt % Pt loading) were also evaluated for comparison. Catalyst N−C, N−C@CNT, and Fe-CNT were obtained by pyrolyzing PDA, PDA@CNT, and Fe_3O_4/CNT, which were prepared in parallel with Fe−N−C@CNT, respectively (see Experimental Section for details). As shown in Figure 3a, the catalytic activities for ORR of N−C, N−C@CNT, and Fe-CNT were much worse than the Fe−N−C@CNT and Pt/C in terms of negative onset-potential and half-wave potential in LSV curves. The better performance of N−C@CNT than N−C can be attributed to the improved electron transfer from CNT network as well as the CNT support effect for better mass transfer. Comparing the LSV curves of Fe−N−C@CNT and N−C@CNT, the former exhibited 107 mV positive shift of the onset-potential and 119 mV positive shift of half-wave potential, as well as a much larger diffusion limiting current density, indicating that the introduction of iron carbide nanocrystals inside the porous N−C shell dramatically enhanced the electrocatalytic activity for ORR. The much improved ORR activity of Fe−N−C@CNT vs Fe-CNT corroborated that the synergetic effect of iron carbide nanocrystals and CN_x layer produced the more efficient catalytically active sites for ORR. To understand the ORR process on Fe−N−C@CNT catalyst, the electron transfer process was further investigated by rotating ring-disk electrode (RRDE) experiment. The potential at platinum ring of RRDE was set at 0.5 V (vs Ag/AgCl) to detect peroxide species forming at disk electrode. Figure 3b showed that the H_2O_2 yield on Fe−N−C@CNT catalyst remained below 9% over the potential range from −0.2 to −0.7 V (vs Ag/AgCl), corresponding to an electron-transfer number of over 3.8. This result revealed that ORR on Fe−N−C@CNT catalyst followed by a favorable four-electron process. The Tafel curves were also plotted in Figure S3 (SI) to further evaluate the catalytic activity for ORR. The Tafel slope of the Fe−N−C@CNT catalyst at low overpotentials (87 mV dec^{-1}) is similar to that of Pt/C catalyst (83 mV dec^{-1}), corroborating the excellent catalytic activity of Fe−N−C@CNT.

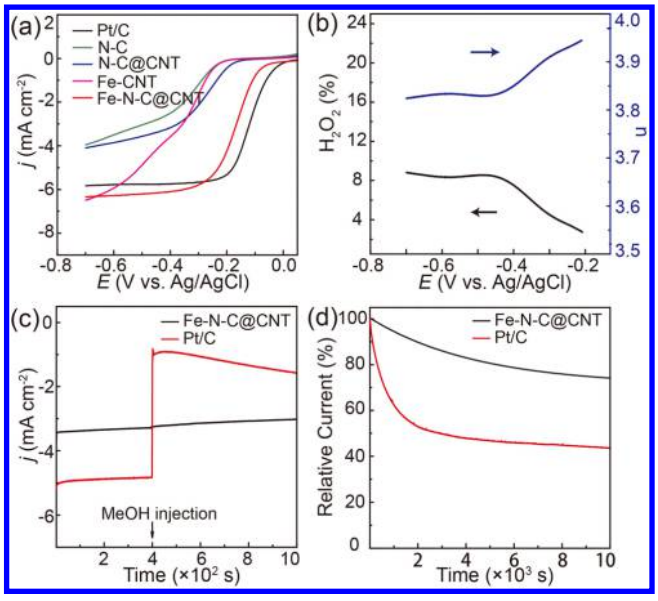

Figure 3. (a) LSV curves of N−C, N−C@CNT, Fe-CNT, Fe−N−C@CNT, and reference Pt/C recorded in O_2-saturated 0.1 M KOH at a scan rate of 10 mV s^{-1} and a rotation speed of 1600 rpm. (b) H_2O_2 yield and electron transfer number (n) in RRDE measurement of Fe−N−C@CNT. (c) Current−time (i−t) chronoamperometric responses of Fe−N−C@CNT and Pt/C recorded at −0.2 V in 0.1 M O_2-saturated KOH solution. The arrow indicates the addition of methanol. (d) Relative current−time (i−t) chronoamperometric responses of Fe−N−C@CNT and Pt/C recorded at −0.2 V in 0.1 M O_2-saturated KOH solution.

The durability of electrocatalysts is critical for its practical application in fuel cells. Methanol crossover is one of the big issues in direct methanol fuel cells, in which methanol can penetrate through proton exchange membrane and thus deteriorate cathode catalysts. Therefore, the present Fe−N−C@CNT was first evaluated for the tolerances of methanol and compared with Pt/C catalyst. As shown in Figure 3c, the cathodic current of Fe−N−C@CNT did not change much after the addition of methanol into electrolyte while that of Pt/C catalyst sharply dropped by 80.35%, which indicated that methanol crossover did not affect the ORR activity of Fe−N−C@CNT. On the other hand, the durability of Fe−N−C@CNT in ORR was further investigated by chronoamperometric measurement. The relative current−time curve of Fe−N−C@CNT (Figure 3d) exhibited a much slower current attenuation than that of Pt/C; 74.17% current remained for Fe−N−C@CNT after 10000 s test, while only 43.56% current left for Pt/C, revealing that Fe−N−C@CNT demonstrated much better durability in ORR than Pt/C.

Furthermore, we noticed that the pyrolysis temperature could influence the catalytic activity of Fe−N−C@CNT catalysts because it would affect the state of catalytic sites. During the preparation of the above-mentioned Fe−N−C@CNT catalyst, which was pyrolyzed at 800 °C, two other Fe−N−C@CNT catalysts were synthesized in parallel at the same conditions except at pyrolysis temperatures of 700 and 900 °C. XRD patterns of three catalysts in Figures 2d and 4a,b show that the three catalysts exhibited the difference in crystalline structure. For the catalyst pyrolyzed at 700 °C, two major diffraction peaks 44.67 and 65.02° can be well indexed to cubic Fe (JCPDS no. 06-0696) and the other three small peaks at 35.63, 43.28, and 50.00° can be attributed to cubic Fe_3O_4 (JCPDS no. 39-1346), indicating the element Fe existed mainly in form of iron with a small amount of Fe_3O_4. In the catalyst

DOI: 10.1021/acsami.5b02467
ACS Appl. Mater. Interfaces 2015, 7, 11508−11515

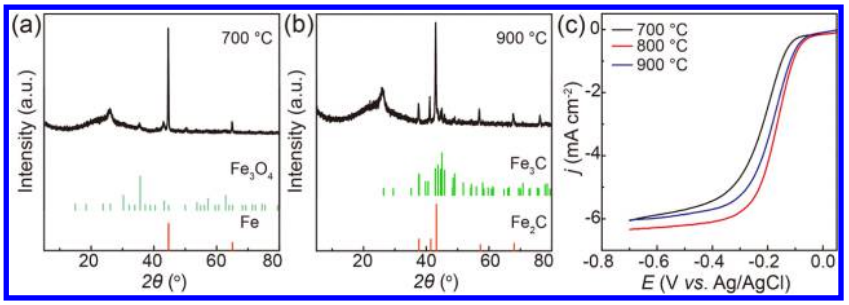

Figure 4. XRD patterns of Fe−N−C@CNT prepared at (a) 700 and (b) 900 °C. (c) LSV curves of Fe−C−N@CNT prepared at various pyrolysis temperature. All LSV curves recorded in O_2-saturated 0.1 M KOH at a scan rate of 10 mV s^{-1} and a rotation speed of 1600 rpm.

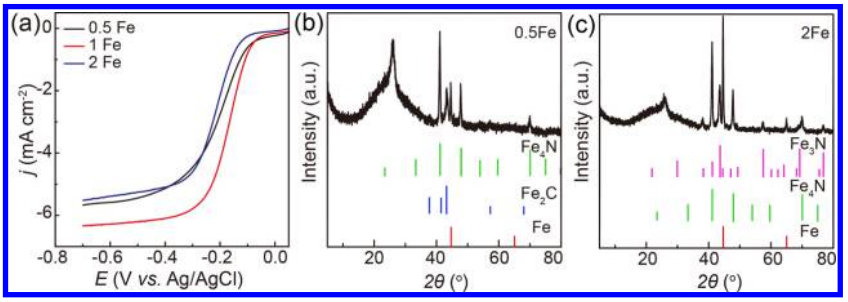

Figure 5. (a) LSV curves and (b and c) XRD patterns of Fe−C−N@CNT catalysts prepared at 800 °C with various amount of iron source. All LSV curves recorded in O_2-saturated 0.1 M KOH at a scan rate of 10 mV s^{-1} and a rotation speed of 1600 rpm.

pyrolyzed at both 800 and 900 °C, all XRD peaks can be indexed to hexagonal Fe_2C and orthorhombic Fe_3C except the peak of graphitized carbon at 26.60°, but the composition ratios of Fe_2C and Fe_3C in two catalysts were slightly different. In all XRD measurements, the materials' loading and recording parameters were carefully kept constant. Comparing the XRD patterns in Figures 2f and 4b, it can be calculated that the intensity ratio of the strongest XRD peaks of Fe_3C to Fe_2C (XRD peak at 44.9° for Fe_3C and peak at 43.1° for Fe_2C) in Fe−N−C@CNT prepared at 800 °C were significantly larger than that of the material prepared at 900 °C (0.58 vs 0.20). In view of the same total iron content in two samples and given that almost all iron compounds were in crystallized form (as indicated in TEM observation), it could be inferred that the relative content of Fe_3C in Fe−N−C@CNT prepared at 800 °C was higher than that in the catalyst prepared at 900 °C, although XRD is not a quantitative analysis. The electrocatalytic performances of three catalysts were subsequently evaluated. As shown in polarization curves in Figure 4c, Fe−N−C@CNT pyrolyzed at 800 °C exhibited the highest activity for ORR in terms of positively shifted onset potential and half-wave potential. The difference in catalytic activity can be ascribed to the difference in the graphitization, composition, and status of iron compounds in these three catalysts. The higher pyrolysis temperature favored the graphitization and thus the electron transport during ORR, but too high a temperature would cause the separation of iron compounds from the carbon support, which degraded the performance of the catalyst. As shown in Figure S5 (SI), the iron carbides separated out and severely aggregated in the catalyst prepared at 900 °C.

In addition, the effect of iron content on ORR performance of Fe−N−C@CNT catalyst was further investigated. Compared to the above-mentioned Fe−N−C@CNT catalyst (800 °C), two more Fe−N−C@CNT catalysts were prepared in parallel except for using half and double amounts of iron source instead. The three catalysts were denoted as 1Fe, 0.5Fe, and 2Fe in Figure 5a. It can be seen that the catalyst 1Fe exhibited the best electrocatalytic activity for ORR. The amount of iron affected not only the amount of active sites, but also the composition of iron compounds. As shown in Figure 5b,c, Fe_4N and Fe_2C dominated in the catalyst 0.5 Fe, while metallic Fe, Fe_4N, and Fe_3N existed in the catalyst 2Fe. By comparing the electrochemical results of the catalysts prepared at different temperatures, it can be concluded that the composition of iron compounds appreciably affected the catalytic performance of the catalysts and Fe_3C might be most effective on improving ORR activity of Fe−N−C@CNT catalysts.

The thickness of CN_x shell also influenced the catalyst performance, which can be controlled by the PDA polymerization time (Figure S1b, SI). The PDA shell around 30 nm thick delivered the best performance in our experiments. A too-thick CN_x shell weakened the electronic interaction between iron compounds and CN_x shell and deteriorated the effective electron transfer from CNT cores, as demonstrated by the inferior ORR activity of the catalyst with 90 nm thick PDA (Figure S5, SI). On the other hand, it was difficult to confine the iron carbides inside the CN_x shell if the shell was not thick enough, which also downgraded the performance of the Fe−N−C@CNT catalysts.

CONCLUSION

In summary, a new type of non-noble-metal nanostructure with core−shell CN_x@CNT structure and encapsulated iron carbide nanocrystals was developed as an efficient electrocatalyst for ORR. Ascribed to the confinement effect of carbonaceous shell during pyrolysis, iron carbide nanocrystals were well dispersed inside the N-doped carbon shell and produced sufficient highly active sites for ORR. The investigation of synthetic conditions on the catalytic activity indicated that the types of iron compounds appreciably affected the catalytic performance of the catalysts. Benefited from the well-defined structure and the composition control of iron compounds, the designed Fe−N−

DOI: 10.1021/acsami.5b02467
ACS Appl. Mater. Interfaces 2015, 7, 11508−11515

C@CNT catalyst demonstrated the superior electrocatalytic activity for ORR with high durability and methanol tolerance.

EXPERIMENTAL SECTION

Synthesis of Fe_3O_4/CNT. In a typical synthesis, 233.4 mg $Fe(acac)_3$ (Alfa Aesar) and 80 mg CNT (Shenzhen Nanotech Port Ltd. Co, China) were ultrasonically dispersed in 48 mL triethylene glycol (Alfa Aesar) in a three-necked flask. The suspension was then heated at 190 °C for 30 min under argon protection and then refluxed at 278 °C for another 30 min. After cooling to room temperature, the product was washed with ethyl acetate several times and dried at 40 °C in vacuum to obtain Fe_3O_4/CNT.

Synthesis of PDA@ Fe_3O_4/CNT. In a typical synthesis of PDA@ Fe_3O_4/CNT, 40 mg Fe_3O_4/CNT was dispersed in a mixed solution of 30 mL of water and 80 mL of ethanol under magnetic stirring for 2 h. Then, 40 mL of aqueous solution of tris-base (100 mM, Alfa Aesar) was added into the suspension. After the addition of 30 mL of aqueous solution containing 160 mg of dopamine, the resultant solution was gently stirred for 6 h at room temperature. The product was filtered, washed with water and ethanol, and then dried overnight at 60 °C.

Synthesis of Fe−N−C@CNT Catalyst. The as-obtained PDA@ Fe_3O_4/CNT was heated to 800 °C under argon atmosphere at a rate of 5 °C/min and then kept at 800 °C for 1 h to achieve Fe−N−C@ CNT after the pyrolysis of PDA.

Synthesis of N−C Catalyst. N−C catalyst was prepared in parallel with the same method as that for Fe−N−C@CNT, except there was no addition of Fe_3O_4/CNT.

Synthesis of Fe-CNT Catalyst. Fe-CNT catalyst was prepared in parallel with the same method as that for Fe−N−C@CNT, except we used Fe_3O_4/CNT instead of PDA@Fe_3O_4/CNT.

Synthesis of N−C@CNT Catalyst. N−C@CNT catalyst was prepared in parallel with the same method as that for Fe−N−C@ CNT, except we used CNT instead of Fe_3O_4/CNT.

Characterization. The morphologies of all materials were characterized by scanning electron microscope (JSM 6701, JEOL, Japan) operated at 10 kV and transmission electron microscope (JEM-2100F, JEOL, Japan) worked at an accelerating voltage of 200 kV. X-ray photoelectron spectroscopy (XPS) spectra were recorded on a VG ESCALab220i-XL with a monochromic Mg Kα source. X-ray diffraction (XRD) experiments were carried out on a Regaku D/ Max-2500 diffractometer equipped with a Cu Kα1 radiation (λ = 1.54056 Å, Rigaku Corporation, Tokyo, Japan). The FTIR spectra were recorded on a TENSOR-27 550II FTIR spectrometer. Nitrogen adsorption−desorption isotherms were measured on the Quadrasorb SI-MP at 77 K. The specific surface areas were calculated by the Brunauer−Emmett−Teller (BET) method, and the pore size distribution curves were calculated by the density functional theory (DFT) method.

Electrochemical Measurements. All electrochemical measurements were recorded on a rotating ring-disk electrode rotator (RRDE-3A, ALS, Japan) by a standard three electrode cell system connected to an electrochemical workstation (CHI 760E, ChenHua, Shanghai, China) at room temperature. A rotating ring disk electrode (RRDE, 4 mm in diameter) coated with catalyst was used as the work electrode. Pt foil and standard Ag/AgCl (3 M KCl solution) reference electrode were used as counter electrode and reference electrode, respectively. RRDE was mechanically polished prior to use with 0.5−0.7 μm and then 0.03−0.05 μm alumina slurry to obtain a mirror-like surface, followed by washing with ethanol and drying in air. For preparation of working electrode, 2 mg of catalyst was dispersed in 800 μL of ethanol and then sonicated for 15 min to obtain a homogeneous ink. Then, 30.2 μL of ink was slowly dropped onto clean glassy carbon electrode to achieve a catalyst loading of 600 μg cm^{-2}. After that, 2 μL nafion (0.5 wt %) solution was dropped onto the electrode surface. After drying in air, the electrode was ready for testing. Commercial Johnson−Matthey Pt/C with 20 wt % Pt loading was used for comparison, and Pt loading on electrode was 25.5 μg cm^{-2}.

Four-electron selectivity of catalyst was evaluated based on H_2O_2 yield, which was calculated from the following equation:

$$H_2O_2\ (\%) = 200 \times \frac{I_R/N}{(I_R/N) + I_D}$$

The electron transfer number (n) was calculated from the following equation:

$$n = 4 \times \frac{I_D}{(I_R/N) + I_D}$$

Where, I_D and I_R are the disk and ring currents, respectively, and N is the ring collection efficiency and equals 0.424.

ASSOCIATED CONTENT

Supporting Information

TEM images of PDA@Fe_3O_4/CNT with 90 nm thick PDA shell and its pyrolyzed product, Fe−C−N@CNT prepared at 900 °C; high-magnification SEM image, Tafel plot of Fe−N−C@CNT; and LSV curves of Fe−C−N@CNT catalysts prepared with PDA shell in various thickness. The Supporting Information is available free of charge on the ACS Publications website at DOI: 10.1021/acsami.5b02467.

AUTHOR INFORMATION

Corresponding Authors

*Email: hujs@iccas.ac.cn.

*Email: zdwei@cqu.edu.cn.

Notes

The authors declare no competing financial interest.

ACKNOWLEDGMENTS

We acknowledge the financial supports from the National Key Project on Basic Research (2015CB932302, 2012CB215500, and 2011CB808701), the National Natural Science Foundation of China (91127044 and 21173237), and the Strategic Priority Research Program of the Chinese Academy of Sciences (Grant No. XDB12020100).

REFERENCES

(1) Gasteiger, H. A.; Markovic, N. M. Chemistry. Just a Dream—or Future Reality? *Science* **2009**, *324*, 48−49.

(2) Jiang, W. J.; Hu, J. S.; Zhang, X.; Jiang, Y.; Yu, B. B.; Wei, Z. D.; Wan, L. J. In Situ Nitrogen-Doped Nanoporous Carbon Nanocables as an Efficient Metal-Free Catalyst for Oxygen Reduction Reaction. *J. Mater. Chem. A* **2014**, *2*, 10154−10160.

(3) Wang, D.; Xin, H. L.; Hovden, R.; Wang, H.; Yu, Y.; Muller, D. A.; DiSalvo, F. J.; Abruña, H. D. Structurally Ordered Intermetallic Platinum−Cobalt Core−Shell Nanoparticles with Enhanced Activity and Stability as Oxygen Reduction Electrocatalysts. *Nat. Mater.* **2013**, *12*, 81−87.

(4) Stamenkovic, V. R.; Fowler, B.; Mun, B. S.; Wang, G.; Ross, P. N.; Lucas, C. A.; Marković, N. M. Improved Oxygen Reduction Activity on $Pt_3Ni(111)$ via Increased Surface Site Availability. *Science* **2007**, *315*, 493−497.

(5) Liu, M.; Zhang, R.; Chen, W. Graphene-Supported Nanoelectrocatalysts for Fuel Cells: Synthesis, Properties, and Applications. *Chem. Rev.* **2014**, *114*, 5117−5160.

(6) Wu, G.; Zelenay, P. Nanostructured Nonprecious Metal Catalysts for Oxygen Reduction Reaction. *Acc. Chem. Res.* **2013**, *46*, 1878−1889.

(7) Wang, D.-W.; Su, D. Heterogeneous Nanocarbon Materials for Oxygen Reduction Reaction. *Energy Environ. Sci.* **2014**, *7*, 576−591.

(8) Yin, S.; Cai, M.; Wang, C.; Shen, P. K. Tungsten Carbide Promoted Pd−Fe as Alcohol-Tolerant Electrocatalysts for Oxygen Reduction Reactions. *Energy Environ. Sci.* **2011**, *4*, 558−563.

(9) Wang, Y.; Song, S.; Maragou, V.; Shen, P. K.; Tsiakaras, P. High Surface Area Tungsten Carbide Microspheres as Effective Pt Catalyst Support for Oxygen Reduction Reaction. *Appl. Catal., B* **2009**, *89*, 223−228.

DOI: 10.1021/acsami.5b02467
ACS Appl. Mater. Interfaces 2015, 7, 11508−11515

(10) Meng, H.; Shen, P. K. Tungsten Carbide Nanocrystal Promoted Pt/C Electrocatalysts for Oxygen Reduction. *J. Phys. Chem. B* **2005**, *109*, 22705−22709.
(11) Hu, Y.; Zhang, H.; Wu, P.; Zhang, H.; Zhou, B.; Cai, C. Bimetallic Pt−Au Nanocatalysts Electrochemically Deposited on Graphene and Their Electrocatalytic Characteristics Towards Oxygen Reduction and Methanol Oxidation. *Phys. Chem. Chem. Phys.* **2011**, *13*, 4083−4094.
(12) Sun, S.; Zhang, G.; Geng, D.; Chen, Y.; Li, R.; Cai, M.; Sun, X. A Highly Durable Platinum Nanocatalyst for Proton Exchange Membrane Fuel Cells: Multiarmed Starlike Nanowire Single Crystal. *Angew. Chem., Int. Ed.* **2011**, *50*, 422−426.
(13) Sun, S.; Jaouen, F.; Dodelet, J.-P. Controlled Growth of Pt Nanowires on Carbon Nanospheres and Their Enhanced Performance as Electrocatalysts in PEM Fuel Cells. *Adv. Mater.* **2008**, *20*, 3900−3904.
(14) Duan, J.; Zheng, Y.; Chen, S.; Tang, Y.; Jaroniec, M.; Qiao, S. Mesoporous Hybrid Material Composed of Mn_3O_4 Nanoparticles on Nitrogen-Doped Graphene for Highly Efficient Oxygen Reduction Reaction. *Chem. Commun.* **2013**, *49*, 7705−7707.
(15) Cao, B.; Veith, G. M.; Diaz, R. E.; Liu, J.; Stach, E. A.; Adzic, R. R.; Khalifah, P. G. Cobalt Molybdenum Oxynitrides: Synthesis, Structural Characterization, and Catalytic Activity for the Oxygen Reduction Reaction. *Angew. Chem., Int. Ed.* **2013**, *52*, 10753−10757.
(16) Tang, H.; Yin, H.; Wang, J.; Yang, N.; Wang, D.; Tang, Z. Molecular Architecture of Cobalt Porphyrin Multilayers on Reduced Graphene Oxide Sheets for High-Performance Oxygen Reduction Reaction. *Angew. Chem., Int. Ed.* **2013**, *52*, 5585−5589.
(17) Lee, J. S.; Park, G. S.; Lee, H. I.; Kim, S. T.; Cao, R.; Liu, M.; Cho, J. Ketjenblack Carbon Supported Amorphous Manganese Oxides Nanowires as Highly Efficient Electrocatalyst for Oxygen Reduction Reaction in Alkaline Solutions. *Nano Lett.* **2011**, *11*, 5362−5366.
(18) Zhang, L. F.; Zhang, C. Y. Multifunctional $Co_{0.85}Se$/Graphene Hybrid Nanosheets: Controlled Synthesis and Enhanced Performances for the Oxygen Reduction Reaction and Decomposition of Hydrazine Hydrate. *Nanoscale* **2014**, *6*, 1782−1789.
(19) Ye, T. N.; Lv, L. B.; Li, X. H.; Xu, M.; Chen, J. S. Strongly Veined Carbon Nanoleaves as a Highly Efficient Metal-Free Electrocatalyst. *Angew. Chem., Int. Ed.* **2014**, *53*, 6905−6909.
(20) Poh, H. L.; Šimek, P.; Sofer, Z.; Pumera, M. Sulfur-Doped Graphene via Thermal Exfoliation of Graphite Oxide in H_2S, SO_2, or CS_2 Gas. *ACS Nano* **2013**, *7*, 5262−5272.
(21) Liu, X.; Antonietti, M. Moderating Black Powder Chemistry for the Synthesis of Doped and Highly Porous Graphene Nanoplatelets and Their Use in Electrocatalysis. *Adv. Mater.* **2013**, *25*, 6284−6290.
(22) Zhang, C.; Mahmood, N.; Yin, H.; Liu, F.; Hou, Y. Synthesis of Phosphorus-Doped Graphene and Its Multifunctional Applications for Oxygen Reduction Reaction and Lithium Ion Batteries. *Adv. Mater.* **2013**, *25*, 4932−4937.
(23) Jin, J.; Pan, F.; Jiang, L.; Fu, X.; Liang, A.; Wei, Z.; Zhang, J.; Sun, G. Catalyst-Free Synthesis of Crumpled Boron and Nitrogen Co-Doped Graphite Layers with Tunable Bond Structure for Oxygen Reduction Reaction. *ACS Nano* **2014**, *8*, 3313−3321.
(24) Sun, X.; Zhang, Y.; Song, P.; Pan, J.; Zhuang, L.; Xu, W.; Xing, W. Fluorine-Doped Carbon Blacks: Highly Efficient Metal-Free Electrocatalysts for Oxygen Reduction Reaction. *ACS Catal.* **2013**, *3*, 1726−1729.
(25) Tan, Y. M.; Xu, C. F.; Chen, G. X.; Fang, X. L.; Zheng, N. F.; Xie, Q. J. Facile Synthesis of Manganese-Oxide-Containing Mesoporous Nitrogen-Doped Carbon for Efficient Oxygen Reduction. *Adv. Funct. Mater.* **2012**, *22*, 4584−4591.
(26) Parvez, K.; Yang, S.; Hernandez, Y.; Winter, A.; Turchanin, A.; Feng, X.; Müllen, K. Nitrogen-Doped Graphene and Its Iron-Based Composite as Efficient Electrocatalysts for Oxygen Reduction Reaction. *ACS Nano* **2012**, *6*, 9541−9550.
(27) Wu, Z. S.; Yang, S.; Sun, Y.; Parvez, K.; Feng, X.; Mullen, K. 3D Nitrogen-Doped Graphene Aerogel-Supported Fe_3O_4 Nanoparticles as Efficient Electrocatalysts for the Oxygen Reduction Reaction. *J. Am. Chem. Soc.* **2012**, *134*, 9082−9085.
(28) Chen, Z.; Higgins, D.; Tao, H.; Hsu, R. S.; Chen, Z. Highly Active Nitrogen-Doped Carbon Nanotubes for Oxygen Reduction Reaction in Fuel Cell Applications. *J. Phys. Chem. C* **2009**, *113*, 21008−21013.
(29) Chen, Z.; Higgins, D.; Chen, Z. Nitrogen Doped Carbon Nanotubes and Their Impact on the Oxygen Reduction Reaction in Fuel Cells. *Carbon* **2010**, *48*, 3057−3065.
(30) Liu, J.; Sun, X.; Song, P.; Zhang, Y.; Xing, W.; Xu, W. High-Performance Oxygen Reduction Electrocatalysts Based on Cheap Carbon Black, Nitrogen, and Trace Iron. *Adv. Mater.* **2013**, *25*, 6879−6883.
(31) Ai, K.; Liu, Y.; Ruan, C.; Lu, L.; Lu, G. M. Sp2 C-Dominant N-Doped Carbon Sub-Micrometer Spheres with a Tunable Size: A Versatile Platform for Highly Efficient Oxygen-Reduction Catalysts. *Adv. Mater.* **2013**, *25*, 998−1003.
(32) Tian, J.; Morozan, A.; Sougrati, M. T.; Lefevre, M.; Chenitz, R.; Dodelet, J. P.; Jones, D.; Jaouen, F. Optimized Synthesis of Fe/N/C Cathode Catalysts for PEM Fuel Cells: A Matter of Iron-Ligand Coordination Strength. *Angew. Chem., Int. Ed.* **2013**, *52*, 6867−6870.
(33) Deng, D.; Yu, L.; Chen, X.; Wang, G.; Jin, L.; Pan, X.; Deng, J.; Sun, G.; Bao, X. Iron Encapsulated within Pod-like Carbon Nanotubes for Oxygen Reduction Reaction. *Angew. Chem., Int. Ed.* **2013**, *52*, 371−375.
(34) Liang, J.; Zhou, R. F.; Chen, X. M.; Tang, Y. H.; Qiao, S. Z. Fe−N Decorated Hybrids of CNTs Grown on Hierarchically Porous Carbon for High-Performance Oxygen Reduction. *Adv. Mater.* **2014**, *26*, 6074−6079.
(35) Gupta, S.; Tryk, D.; Bae, I.; Aldred, W.; Yeager, E. Heat-Treated Polyacrylonitrile-Based Catalysts for Oxygen Electroreduction. *J. Appl. Electrochem.* **1989**, *19*, 19−27.
(36) Liang, H. W.; Wei, W.; Wu, Z. S.; Feng, X.; Mullen, K. Mesoporous Metal-Nitrogen-Doped Carbon Electrocatalysts for Highly Efficient Oxygen Reduction Reaction. *J. Am. Chem. Soc.* **2013**, *135*, 16002−16005.
(37) Xiang, Z.; Xue, Y.; Cao, D.; Huang, L.; Chen, J. F.; Dai, L. Highly Efficient Electrocatalysts for Oxygen Reduction Based on 2D Covalent Organic Polymers Complexed with Non-Precious Metals. *Angew. Chem., Int. Ed.* **2014**, *53*, 2433−2437.
(38) Hou, Y.; Huang, T.; Wen, Z.; Mao, S.; Cui, S.; Chen, J. Metal−Organic Framework-Derived Nitrogen-Doped Core-Shell-Structured Porous Fe/Fe_3C@C Nanoboxes Supported on Graphene Sheets for Efficient Oxygen Reduction Reactions. *Adv. Energy Mater.* **2014**, *4*, 1400337.
(39) Yin, H.; Zhang, C.; Liu, F.; Hou, Y. Hybrid of Iron Nitride and Nitrogen-Doped Graphene Aerogel as Synergistic Catalyst for Oxygen Reduction Reaction. *Adv. Funct. Mater.* **2014**, *24*, 2930−2937.
(40) Yao, Y.; Xiao, H.; Wang, P.; Su, P.; Shao, Z.; Yang, Q. CNTs@Fe-N-C Core-Shell Nanostructures as Active Electrocatalyst for Oxygen Reduction. *J. Mater. Chem. A* **2014**, *2*, 11768−11775.
(41) Hu, Y.; Jensen, J. O.; Zhang, W.; Cleemann, L. N.; Xing, W.; Bjerrum, N. J.; Li, Q. Hollow Spheres of Iron Carbide Nanoparticles Encased in Graphitic Layers as Oxygen Reduction Catalysts. *Angew. Chem., Int. Ed.* **2014**, *53*, 3675−3679.
(42) Wen, Z.; Ci, S.; Zhang, F.; Feng, X.; Cui, S.; Mao, S.; Luo, S.; He, Z.; Chen, J. Nitrogen-Enriched Core-Shell Structured Fe/Fe_3C−C Nanorods as Advanced Electrocatalysts for Oxygen Reduction Reaction. *Adv. Mater.* **2012**, *24*, 1399−1404.
(43) Deng, J.; Ren, P.; Deng, D.; Bao, X. Enhanced Electron Penetration through an Ultrathin Graphene Layer for Highly Efficient Catalysis of the Hydrogen Evolution Reaction. *Angew. Chem., Int. Ed.* **2015**, *54*, 2100−2104.
(44) Tavakkoli, M.; Kallio, T.; Reynaud, O.; Nasibulin, A. G.; Johans, C.; Sainio, J.; Jiang, H.; Kauppinen, E. I.; Laasonen, K. Single-Shell Carbon-Encapsulated Iron Nanoparticles: Synthesis and High Electrocatalytic Activity for Hydrogen Evolution Reaction. *Angew. Chem., Int. Ed.* **2015**, *54*, 4535−4538.
(45) Zhou, W.; Zhou, J.; Zhou, Y.; Lu, J.; Zhou, K.; Yang, L.; Tang, Z.; Li, L.; Chen, S. N-Doped Carbon-Wrapped Cobalt Nanoparticles

DOI: 10.1021/acsami.5b02467
ACS Appl. Mater. Interfaces 2015, 7, 11508−11515

on N-Doped Graphene Nanosheets for High-Efficiency Hydrogen Production. *Chem. Mater.* **2015**, *27*, 2026−2032.

DOI: 10.1021/acsami.5b02467
ACS Appl. Mater. Interfaces 2015, 7, 11508−11515